CM² MAGAZINE

第 117 期

南方科技大学海洋磁学中心主编

http://cm2.sustech.edu.cn/

创刊词

海洋是生命的摇篮，是文明的纽带。地球上最早的生命诞生于海洋，海洋里的生命最终进化成了人类，人类的文化融合又通过海洋得以实现。人因海而兴。

人类对海洋的探索从未停止。从远古时代美丽的神话传说，到麦哲伦的全球航行，再到现代对大洋的科学钻探计划，海洋逐渐从人类敬畏崇拜幻想的精神寄托演变成可以开发利用与科学研究的客观存在。其中，上个世纪与太空探索同步发展的大洋科学钻探计划将人类对海洋的认知推向了崭新的纬度：深海（deep sea）与深时（deep time）。大洋钻探计划让人类知道，奔流不息的大海之下，埋藏的却是亿万年的地球历史。它们记录了地球板块的运动，从而使板块构造学说得到证实；它们记录了地球环境的演变，从而让古海洋学方兴未艾。

在探索海洋的悠久历史中，从大航海时代的导航，到大洋钻探计划中不可或缺的磁性地层学，磁学发挥了不可替代的作用。这不是偶然，因为从微观到宏观，磁性是最基本的物理属性之一，可以说，万物皆有磁性。基于课题组的学科背景和对海洋的理解，我们对海洋的探索以磁学为主要手段，海洋磁学中心因此而生。

海洋磁学中心，简称 CM^2，一为其全名“Centre for Marine Magnetism”的缩写，另者恰与爱因斯坦著名的质能方程 $E = MC^2$ 对称，借以表达我们对科学巨匠的敬仰和对科学的不懈追求。

然而科学从来不是单打独斗的产物。我们以磁学为研究海洋的主攻利器，但绝不仅限于磁学。凡与磁学相关的领域均是我们关注的重点。为了跟踪反映国内外地球科学特别是与磁学有关的地球科学领域的最新研究进展，海洋磁学中心特地主办 CM^2 Magazine，以期与各位地球科学工作者相互交流学习、合作共进！

“海洋孕育了生命，联通了世界，促进了发展”。21 世纪是海洋科学的时代，由陆向海，让我们携手迈进中国海洋科学的黄金时代。

目录

1. 全新世西南极冰盖融解受控于热带太平洋变暖

翻译人：仲义 zhongy@sustech.edu.cn

Sproson, A.D, Yokoyama, Y., Miyairi, Y., et al. ***Holocene melting of the West Antarctic Ice Sheet driven by tropical Pacific warming*** *[J] Nature Communications, 2022, 13(1), 2434. https://doi.org/10.1038/s41467-022-30076-2*

摘要：南极对现代海平面的贡献主要通过南极冰盖西部的阿蒙森海的冰川释放。造成海冰质量损失的主要过程包括：（1）暖水上涌导致的海洋驱动的冰架融化作用；（2）大气驱动下沿南极海岸附近的冰川融水。了解这些过程对冰川稳定性的相对影响是预测海平面上升的必要条件。作者利用 Be 同位素指标重建了冰架全新世以来变化特征，结果证明，流入到阿蒙森海湾的冰川在 9 千年到 6 千年之间经历了融化和退缩的影响。尽管受到温暖海水的影响，这次融水事件主要是由于西南极洲大陆的大气环流变化造成的，通过罗斯贝波将热带太平洋变暖信号传递到南极地区。这一千年尺度的冰川历史可以用来验证当代冰盖模型，并为海平面预测进行校正。

ABSTRACT: The primary Antarctic contribution to modern sea-level rise is glacial discharge from the Amundsen Sea sector of the West Antarctic Ice Sheet. The main processes responsible for ice mass loss include: (1) ocean-driven melting of ice shelves by upwelling of warm water onto the continental shelf; and (2) atmospheric-driven surface melting of glaciers along the Antarctic coast. Understanding the relative influence of these processes on glacial stability is imperative to predicting sea-level rise. Employing a beryllium isotope-based reconstruction of ice-shelf history, we demonstrate that glaciers flowing into the Amundsen Sea Embayment underwent melting and retreat between 9 and 6 thousand years ago. Despite warm ocean water influence, this melting event was mainly forced by atmospheric circulation changes over continental West Antarctica, linked via a Rossby wave train to tropical Pacific Ocean warming. This millennial-scale glacial history may be used to validate contemporary ice-sheet models and improve sea-level projections.

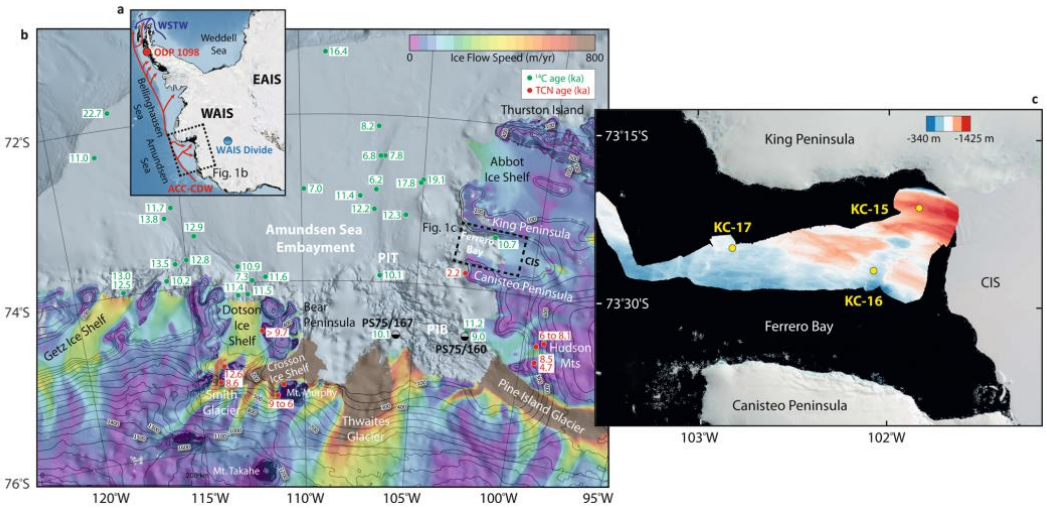

Figure 1. Maps of West Antarctica, the ASE, and Ferrero Bay. a Map of Antarctica displaying a generalised position of Antarctic Circumpolar Current Circumpolar Deep Water (ACC-CSW) and Weddell Sea Transitional Water (WSTW). b Ice velocity, satellite imagery, radiocarbon dates and terrestrial cosmogenic nuclide dates for the Amundsen Sea Embayment, Pine Island Trough (PIT), and Pine Island Bay (PIB). c Location of OSO-0910 KC-15, KC-16, and KC-17 in Ferrero Bay with multibeam swath bathymetry. Maps were constructed using Quantarctica from the Norwegian Polar Institute.

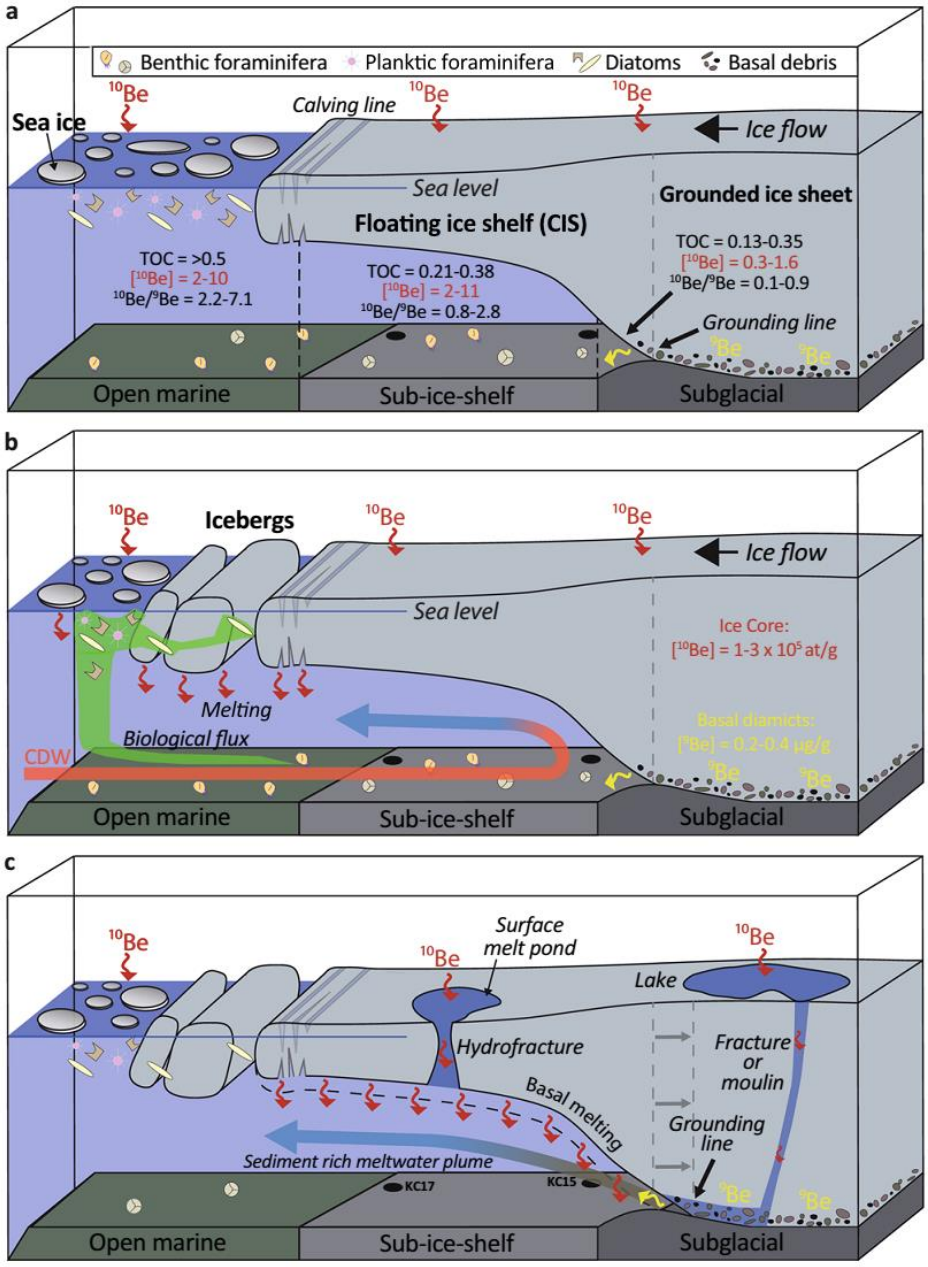

Figure 2. Illustration of the potential processes influencing Be isotopes within Ferrero Bay. a Open marine, sub-ice-shelf, and subglacial environments are defined by different geochemical compositions. b Melting of icebergs and sea ice near the calving line releases ^{10}Be which is rapidly scavenged by diatom frustules and organic matter before becoming advected under the ice-shelf with other marine material by ocean currents such as intruding CDW. c Meltwater rich in ^{10}Be is released from the ice-shelf base and scavenged by fine-grained sediment delivered from the grounding line. This figure was modified from Yokoyama et al. and White et al.

2. 古地磁欧拉极分析的优化方法

翻译人：刘伟 inewway@163.com

Gallo L, Sapienza F, Domeier M, et al. ***An optimization method for paleomagnetic Euler pole analysis*** *[J]. Computers & Geosciences, 2022.*

https://doi.org/ 10.1016/j.cageo.2022.105150

摘要：由于地球磁场的轴向对称性，古地磁数据只能直接记录地质历史时期板块的纬度和方位位置，不能约束古经度。因此，克服这一障碍对古地理重建具有相当的重要性。古地磁欧拉极(PEP)分析提供了一种独特的方法来恢复这些信息。但之前的 PEP 方法在执行过程中加入了主观决策，降低了其可靠性和严谨性。在这里，我们提出了一种 PEP 分析的优化方法，解决了其中的一些缺陷，即客观地识别变化点和小圆弧，它们一起近似于一个视极移曲线。我们详细阐述了我们的新方法，并利用综合的数据进行了实验，以证明其性能。此外，我们还将我们的方法实现为可适应的、独立的 Python 脚本，以及可以通过 web 浏览器操作的网页。

ABSTRACT: Owing to the axial symmetry of the Earth's magnetic field, paleomagnetic data only directly record the latitudinal and azimuthal positions of crustal blocks in the past, and paleolongitude cannot be constrained. An ability to overcome this obstacle is thus of fundamental importance to paleogeographic reconstruction. Paleomagnetic Euler pole (PEP) analysis presents a unique means to recover such information, but prior implementations of the PEP method have incorporated subjective decisions into its execution, undercutting its fidelity and rigor. Here we present an optimization approach to PEP analysis that addresses some of these deficiencies—namely the objective identification of change-points and small-circle arcs that together approximate an apparent polar wander path. We elaborate on our novel methodology and conduct some experiments with synthetic data to demonstrate its performance. We furthermore present implementations of our methods both as adaptable, stand-alone scripts in Python and as a streamlined interactive workflow that can be operated through a web browser.

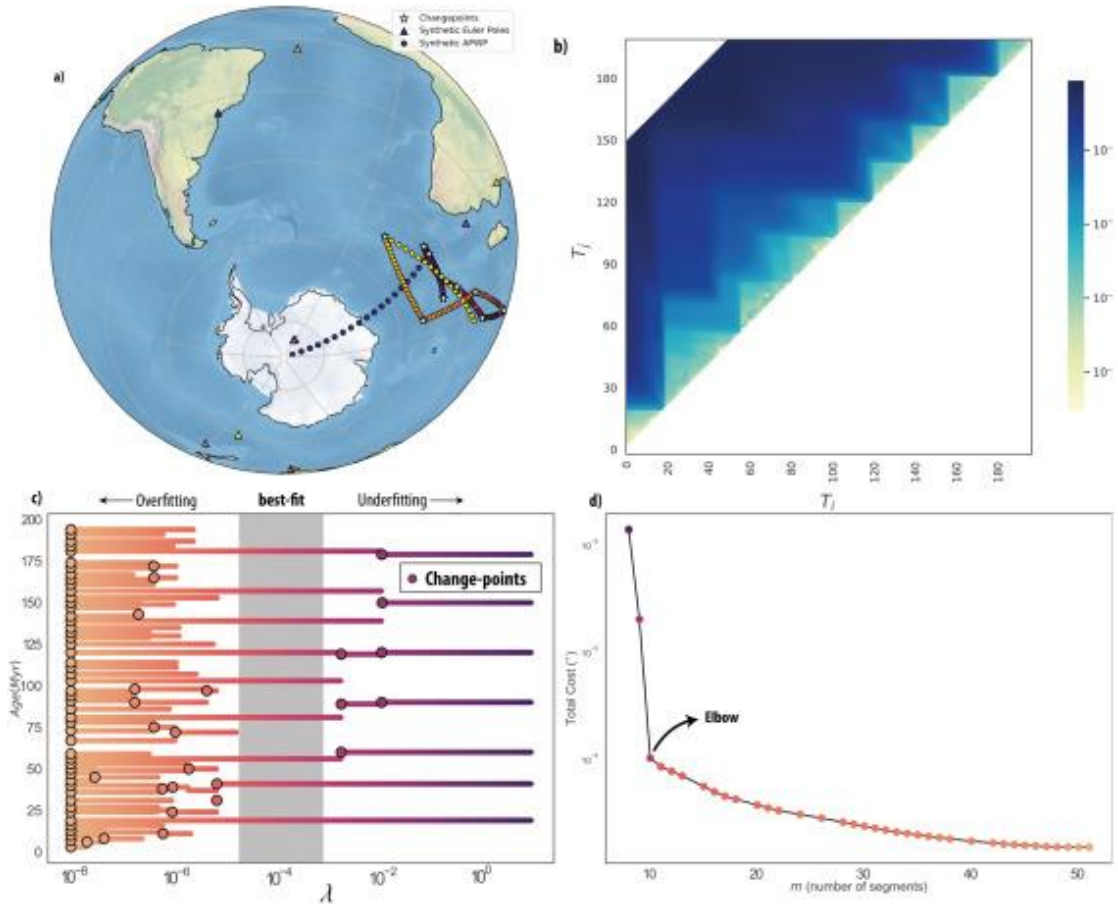

Figure 1. Graphical illustration of the application of our methodology. (a) We start by generating a stochastic model of the drift of a plate over 200 Ma by randomly generating stage Euler vectors (triangles). From this stochastic kinematic model, we assemble a synthetic APWP (dots) populated by paleomagnetic poles every 1 My. (b) Heatmap visualization of the adjacency matrix illustrating the magnitude of the cost function for each candidate APWP segment.(c) Scatter plot illustration of the number of change-points per age (dots) as a function of an increasing hyperparameter λ. Large values of λ increase the value of the cost function, such that a good-fitting APWP with fewer segments will be favored. (d) Scatter plot illustrating the elbow method: the total cost (y axis) is plotted against the number of segments (x axis), color coded by the hyperparameter λ. The graphical 'elbow' in the plot thus points to this optimal value of λ.

3. 中国东南部仙云洞在 Heinrich1 事件期间记录的东亚夏季风的双骤降结构

翻译人：杨会会 11849590@mail.sustech.edu.cn

Qiu W Y, Zhang X , Jiang X Y, et al., ***Double-plunge structure of the East Asian summer monsoon during Heinrich stadial 1 recorded in Xianyun Cave, southeastern China [J].*** *Quaternary Science Reviews, 2022, 282, 107442*

https://doi.org/10.1016/j.quascirev.2022.107442

摘要：季风降水在千年尺度上的半球间反相位关系已被广泛证实，通常归因于热带辐合带(ITCZ) 平均位置的迁移。然而，之前的高分辨率记录表明，半球间季风气候可能在 Heinrich 事件 1 (HS1) 期间解耦，造成了亚洲夏季风的“双重细分”，和南美夏季风的“双重骤降”结构。本研究利用中国东南部，受东亚夏季风(EASM)影响的锋面区域，获取的高分辨率、精确年代的石笋氧同位素记录，呈现了在 HS1 期间明显的双骤降结构。我们的新记录特征是在 HS1 对应的弱 EASM 期，分为两个弱期 (HS1c, 17.89-17.01 ka B.P.; HS1a, 15.94-14.76 ka B.P.)被一个相对强的阶段(HS1b, 17.01-15.94 ka B.P.) 分割开。与来自全球季风系统的其他记录的比较表明，HS1 期间的双骤降结构广泛分布于低纬度季风区，并且在亚千年尺度上，季风水文气候的半球间反位相关系仍然存在。这种结构可能与北大西洋的两个融水脉冲密切相关，它们被一段较弱的时期和淡水入海口地点的短暂改变分隔开。淡水入海口地点的短暂改变指的是，由劳伦特冰盖产生的淡水由从亚极地北部输入北大西洋，改道至从墨西哥湾注入低纬度大西洋。HS1b 期间半球间热梯度的变化可能短暂地拉动/推动了 ITCZ 北移，并引起了半球间季风气候的同步和反向变化。

ABSTRACT: The interhemispheric anti-phase relationship of monsoon precipitation on the millennial timescale has been widely verified and is generally attributed to the migration of the mean position of the Intertropical Convergence Zone (ITCZ). However, previous high-resolution records showed that the interhemispheric monsoon climate could have been decoupled within Heinrich stadial 1 (HS1), creating a two-fold subdivision in the Asian summer monsoon and a

double-plunge structure in the South American summer monsoon. In this study, we present a high-resolution and precisely dated composite stalagmite oxygen isotope record exhibiting a clear double-plunge structure during HS1 from southeastern China, the frontal zone predominantly influenced by the East Asian summer monsoon (EASM). Our new record characterizes a weak EASM period corresponding to HS1, divided into two weak periods (HS1c, 17.89-17.01 ka B.P.; HS1a, 15.94-14.76 ka B.P.) by a relatively strong phase (HS1b, 17.01-15.94 ka B.P.). Comparisons with other records from global monsoon systems suggest the double-plunge structure of HS1 is widespread in the low latitudes of monsoon domains, and the interhemispheric anti-phase relationship of the monsoonal hydroclimate still holds on the sub-millennial timescale. This structure could be closely linked with two meltwater pulses in the North Atlantic, separated by a weak period and a brief rerouting of the main freshwater input produced by the Laurentide ice sheet from subpolar North Atlantic to the Gulf of Mexico. The change in the interhemispheric thermal gradient during HS1b likely pulled/pushed the ITCZ northward briefly and induced the synchronous and reverse change in the interhemispheric monsoon climate.

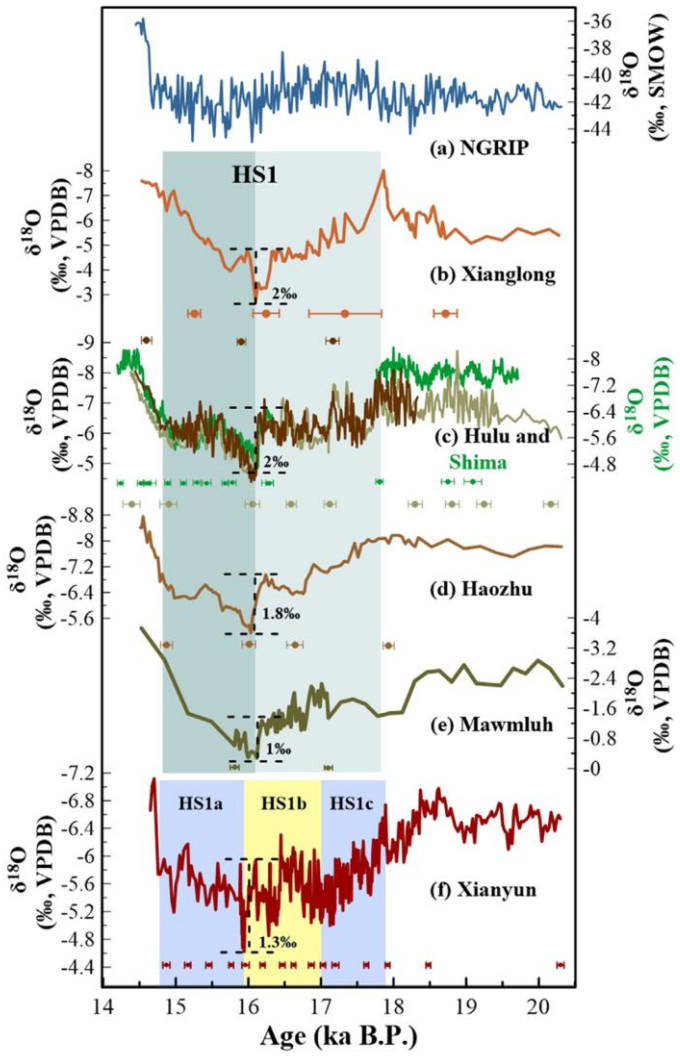

Figure 1. (a) Comparison between (a) $\delta^{18}O$ record of NGRIP ice core (North Greenland Ice Core Project Members, 2004) and stalagmite $\delta^{18}O$ records from Asian monsoon realm. Caves are (b) Xianglong Cave from central China (Li et al., 2019); (c) YT (walnut, Wang et al., 2001; Zhang et al., 2014) and H82 (khaki, Wang et al., 2001; Wu et al., 2009) of Hulu Cave, and Shima Cave (grass green) (Liang et al., 2020) from the middle and lower reaches of the Yangtze River; (d) Haozhu Cave from the middle and lower reaches of the Yangtze River (Zhang et al., 2016); (e) Mawmluh Cave, India (Dutt et al., 2015); and (f) Xianyun Cave, southeastern China (This study). The numbers denote the relative $\delta^{18}O$ changes during the classical H1 shift. Light and deep ocean green verticals bars express the two-fold structure of HS1 according to Liang et al. (2020). Baby blue and yellow vertical bars show the subphases of HS1a, HS1b, and HS1c.

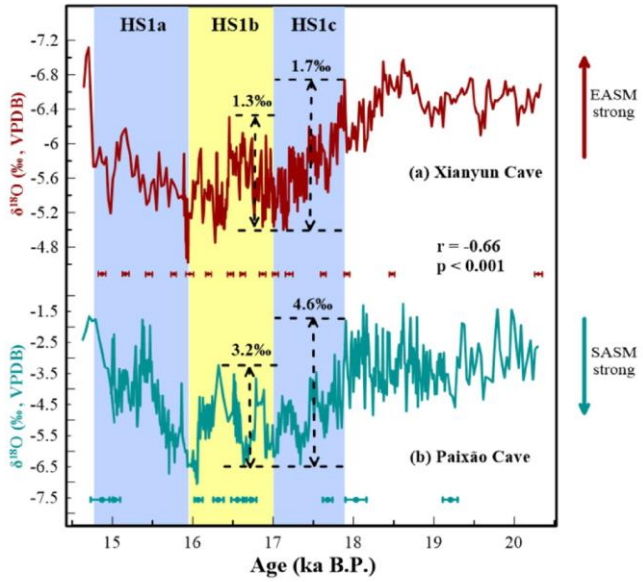

Figure 2. Comparison of (a) Xianyun $\delta^{18}O$ record of the EASM (this study) and (b) Paixao $\delta^{18}O$ record of the SASM (Stríkis et al., 2015, 2018). Note the reversed y-axis in the Xianyun $\delta^{18}O$ record. The numbers above the dotted line denote the relative changes of $\delta^{18}O$ during HS1c and the increasing phase of HS1b (17.01-16.45 ka B.P.). The correlation coefficient of -0.66 ($p < 0.001$) shows a significant inverse correlation between the two records with independent chronologies at HS1. Blue and yellow shading delimit the intervals of HS1a, HS1b, and HS1c.

4. 过去 4 个百万年以来南大洋风尘与气候的耦合演变

翻译人：王敦繁 Dunfan-w@foxmail.com

Alfredo, M. G., Antoni, R. M., Samuel, L. J., Walter, G. et al. ***Southern Ocean dust-climate coupling over the past four million years [J]***. *Nature* 2011; 312, 476.

https://doi.org/10.1038/nature10310

摘要：风尘有可能改变全球气候，影响大气的辐射平衡，并向海洋提供铁和其他必要的限制性微量营养素。事实上，冰河期期间，南大洋的风尘供应增加，亚南极带的“铁肥”可能对晚更新世冰川旋回期间观测到的大气二氧化碳减少量（80-100 p.p.m.v.）的贡献高达百万分之四十（p.p.m.v.）。然而，迄今为止，早期南大洋尘埃沉积的规模及其在更新世冰川旋回的发展和演化中的作用仍不清楚。在这里，我们报告了过去 400 万年来南大洋尘埃和铁供应的高分辨率记录，该记录来自对位于亚南极区大西洋部分的 ODP 1090 现场的海洋沉积物的分析。我们的尘埃和铁沉积记录与过去 80 万年南极冰芯尘埃通量重建的密切对应表明，这两个档案记录了大规模沉积变化，应适用于大部分南大洋，验证了以前对冰芯数据的解释。记录的延伸超出了南极冰芯覆盖的时间间隔，这表明，与过去 300 万年相对逐渐加剧的冰川周期相比，大约 125 万年前，在中更新世气候转变期间，南大洋的尘埃和铁通量急剧上升。这一发现补充了之前对晚更新世冰川旋回的观察，提供了新的证据，证明南大洋的高尘埃输入与过去一百万年地球历史中深冰川的出现之间存在着紧密联系。

ABSTRACT: Dust has the potential to modify global climate by influencing the radiative balance of the atmosphere and by supplying iron and other essential limiting micronutrients to the ocean, indeed, dust supply to the Southern Ocean increases during ice ages, and ‘iron fertilization’ of the subantarctic zone may have contributed up to 40 parts per million by volume (p.p.m.v.) of the decrease (80–100 p.p.m.v.) in atmospheric carbon dioxide observed during late Pleistocene glacial cycles. So far, however, the magnitude of Southern Ocean dust deposition in earlier times and its role in the development and evolution of Pleistocene glacial cycles have remained unclear. Here we report a high-resolution record of dust and iron supply to the Southern Ocean over the past four million years, derived from the analysis of marine sediments from ODP Site 1090, located in the

Atlantic sector of the subantarctic zone. The close correspondence of our dust and iron deposition records with Antarctic ice core reconstructions of dust flux covering the past 800,000 years indicates that both of these archives record large-scale deposition changes that should apply to most of the Southern Ocean, validating previous interpretations of the ice core data. The extension of the record beyond the interval covered by the Antarctic ice cores reveals that, in contrast to the relatively gradual intensification of glacial cycles over the past three million years, Southern Ocean dust and iron flux rose sharply at the Mid- Pleistocene climatic transition around 1.25 million years ago. This finding complements previous observations over late Pleistocene glacial cycles providing new evidence of a tight connection between high dust input to the Southern Ocean and the emergence of the deep glaciations that characterize the past one million years of Earth history.

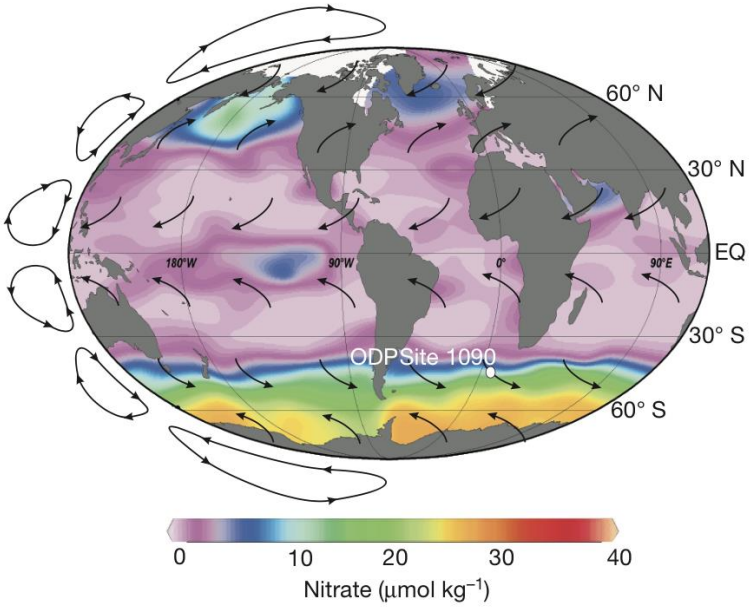

Figure 1. Location of ODP Site 1090, world ocean surface nitrate concentrations, and wind direction. ODP Site 1090, the source of the sediment cores used in this study. Nitrate concentrations are from the Electronic Atlas of the World Ocean Experiment. Black arrows are schematic representations of atmospheric convection cells and wind directions. EQ, Equator.

5. 玉兔二号火星车观测岩石光谱解释的月地模拟实验

翻译人：曹伟 119308540@qq.com

Chang R, Yang W, Lin H, et al. ***Lunar Terrestrial Analog Experiment on the Spectral Interpretations of Rocks Observed by the Yutu-2 Rover*** *[J].* ***remote sensing****, 2022, 14:2323. https://doi.org/10.3390/rs14102323*

摘要：嫦娥四号火星车搭载的可见光和近红外成像光谱仪（VNIS）是探测着陆区月球表面矿物成分的主要方法。然而，不同的数据处理方法在测量月球土壤和岩石中产生了不一致的矿物模式。为了更好地约束嫦娥四号 VNIS 测量土壤和岩石的矿物模式，通过扫描电子显微镜（SEM）、嫦娥四号 VNIS 巡视器和地物光谱仪（TerraSpec-4, ASD）测量了一种矿物成分与月球高地岩石相似的苏长-辉长岩。背散射电子能谱表明，橄榄石、辉石和斜长石模式矿物的丰度分别为 12.9%、35.0%和 52.2%。Hapke 辐射传输模型的光谱结果估计橄榄石、辉石和斜长石的丰度分别为 7.5%、39.3%和 53.2%，这与 SEM 扫描结果在误差范围内一致。相比之下，修正高斯模型估计橄榄石和辉石的结果分别为 29%和 71%，表明不存在斜长石。基于我们应用的 Hapke 模型，我们解译了月球车在执行任务的第 3 和第 26 月昼探测到的两块岩石的数据。所得结果表明，两种岩石均为苏长岩或辉长岩，具有明显差异。第一块含有更多橄榄石和辉石的岩石可能来源于 Finsen 陨石坑。第二块含有更多斜长石的岩石可能来源于 Von Kármán 陨石坑西南边缘，表明初始月壳物质。

ABSTRACT: A visible and near-infrared imaging spectrometer (VNIS) loaded by the Chang'e-4 rover is the primary method for detecting the mineral composition of the lunar surface in the landing region. However, different data processing methods yield inconsistent mineral modes in measured lunar soil and rocks. To better constrain the mineral modes of the soil and rocks measured by Chang'e-4 VNIS, a noritic-gabbroic rock with a mineral composition similar to that of the lunar highland rocks is measured by scanning electron microscopy (SEM), the spare flight model of Chang'e-4 VNIS and TerraSpec-4 of ASD. Backscattered electron and energy dispersive spectrometry show that olivine, pyroxene, and plagioclase modal mineral abundances are 12.9, 35.0, and 52.2%, respectively. The estimated results of the spectrum by the Hapke radiative transfer

model are 7.5, 39.3, and 53.2% for olivine, pyroxene, and plagioclase, respectively, which is consistent with to those of SEM mapping within error. In contrast, the estimated results of the modified Gaussian model are 29 and 71% for olivine and pyroxene, respectively, indicating the absence of plagioclase. Based on our implemented Hapke model, we decode the data of the two rocks detected by the rover on the 3rd and 26th lunar days of mission operations. The obtained results suggest that both rocks are norite or gabbro with noticeable differences. The first rock, with more olivine and pyroxene, may have been excavated from the Finsen crater. The second rock, with more plagioclase, may have been ejected from the southwestern edge of the Von Kármán crater, indicating the initial lunar crust.

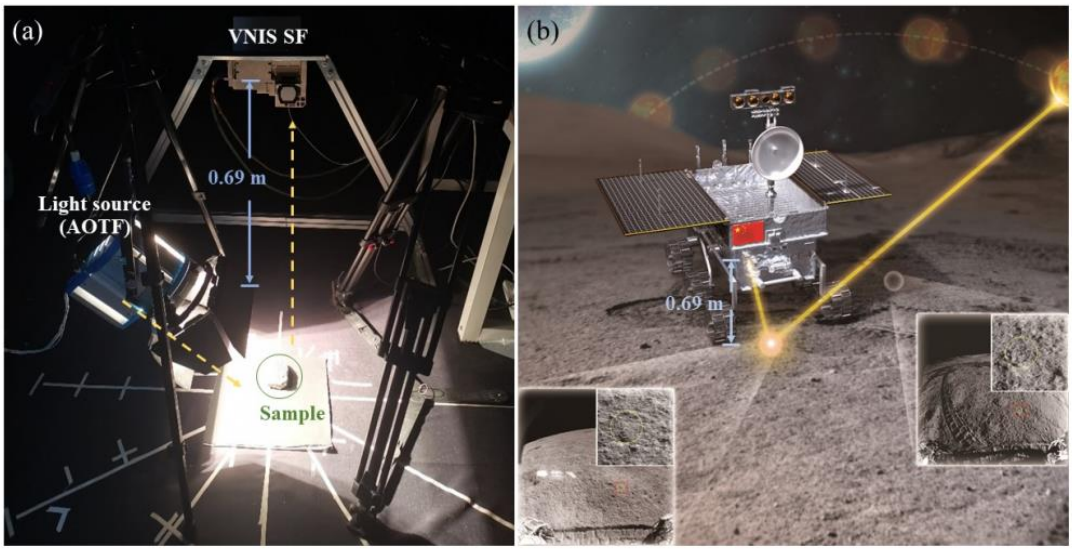

Figure 1. (a) The picture of the VNIS SF experiment condition. (b) The model picture of the detecting condition of VNIS on the lunar surface.

6. 了解生物成因磁铁矿在地磁场古强度记录中的作用：来自 Onton Java 高原沉积物的研究

翻译人：王浩森 11930841@mail.sustech.edu.cn

Li J, Yamazaki T, Usui Y, et al. ***Understanding the Role of Biogenic Magnetite in Geomagnetic Paleointensity Recording: Insights from Ontong Java Plateau Sediments****[J]. Journal of Geophysical Research: Solid Earth, 2022: e2022JB024387.*

https://doi.org/10.1029/2022JB024387

摘要：海洋沉积物可以保存连续的古地磁强度记录。不同的磁性矿物可能获得不同的剩磁，因此沉积物中磁性矿物组合的成分变化可能会阻碍可靠的相对古强度（RPI）记录的提取。为了更好地理解这个问题，我们对赤道西太平洋 Onton Java 高原的一个沉积岩芯进行了古地磁和岩石磁学研究。通过将自然剩磁（NRM）与非磁滞剩磁（ARM）归一化来计算 RPI，与 ARM 磁化率与饱和等温剩磁的比率成反比。这种关系表明，RPI 信号随着生物成因磁铁矿比例的增加而减弱。获得的 NRM-ARM 退磁图具有下凹曲率。这些观察结果表明，如果我们假设高矫顽力部分和低矫顽力部分的磁化分别主要由生物和陆源组分携带，则生物组分的 RPI 记录效率低于陆源组分。这一假设得到了一阶反转曲线测量、透射电镜观察、低温测量以及从沉积物中提取硅酸盐磁性包裹体的支持。以往的研究表明，生物成因磁铁矿的 RPI 记录效率高于陆源组分，这与我们的结果不一致。不同沉积环境中不同浓度的硅酸盐磁性包裹体可能解释了这一矛盾。我们得出结论，生物成因磁铁矿对 RPI 记录的贡献率低于研究沉积物中未受保护的陆源磁性矿物。改变生物成因磁铁矿比例会改变 ARM 归一化 RPI 的计算。

ABSTRACT: Marine sediments can preserve continuous paleomagnetic intensity records. Different magnetic minerals may acquire remanent magnetizations differently, so that compositional variations of magnetic mineral assemblages in sediments may hinder extraction of reliable relative paleointensity (RPI) records. To better understand this issue, we conducted a paleo- and rock magnetic study of a sediment core from the Ontong Java Plateau, western equatorial Pacific Ocean.

RPI estimated by normalizing natural remanent magnetization (NRM) with anhysteretic remanent magnetization (ARM) decreases downcore with an inverse correlation with the ratio of ARM susceptibility to saturation isothermal remanent magnetization. This relationship indicates that the RPI signal weakens as the proportion of biogenic magnetite increases. The NRM–ARM demagnetization diagrams obtained have concave-down curvature. These observations indicate that the RPI recording efficiency of the biogenic component is lower than that of the terrigenous component if we assume that the magnetizations of the high- and low-coercivity windows are carried dominantly by biogenic and terrigenous components, respectively. This assumption is supported by first-order reversal curve measurements, transmission electron microscope observations, low-temperature measurements, and extraction of silicate-hosted magnetic inclusions from the sediments. Previous studies have suggested that the RPI recording efficiency of biogenic magnetite is higher than that of the terrigenous component, which disagrees with our results. Different concentrations of silicate-hosted magnetic inclusions in different sedimentary environments might explain this contradiction. We conclude that biogenic magnetite contributes to RPI records with lower efficiency than unprotected terrigenous magnetic minerals in the studied sediments. Changing biogenic magnetite proportions distort ARM-normalized RPI estimations.

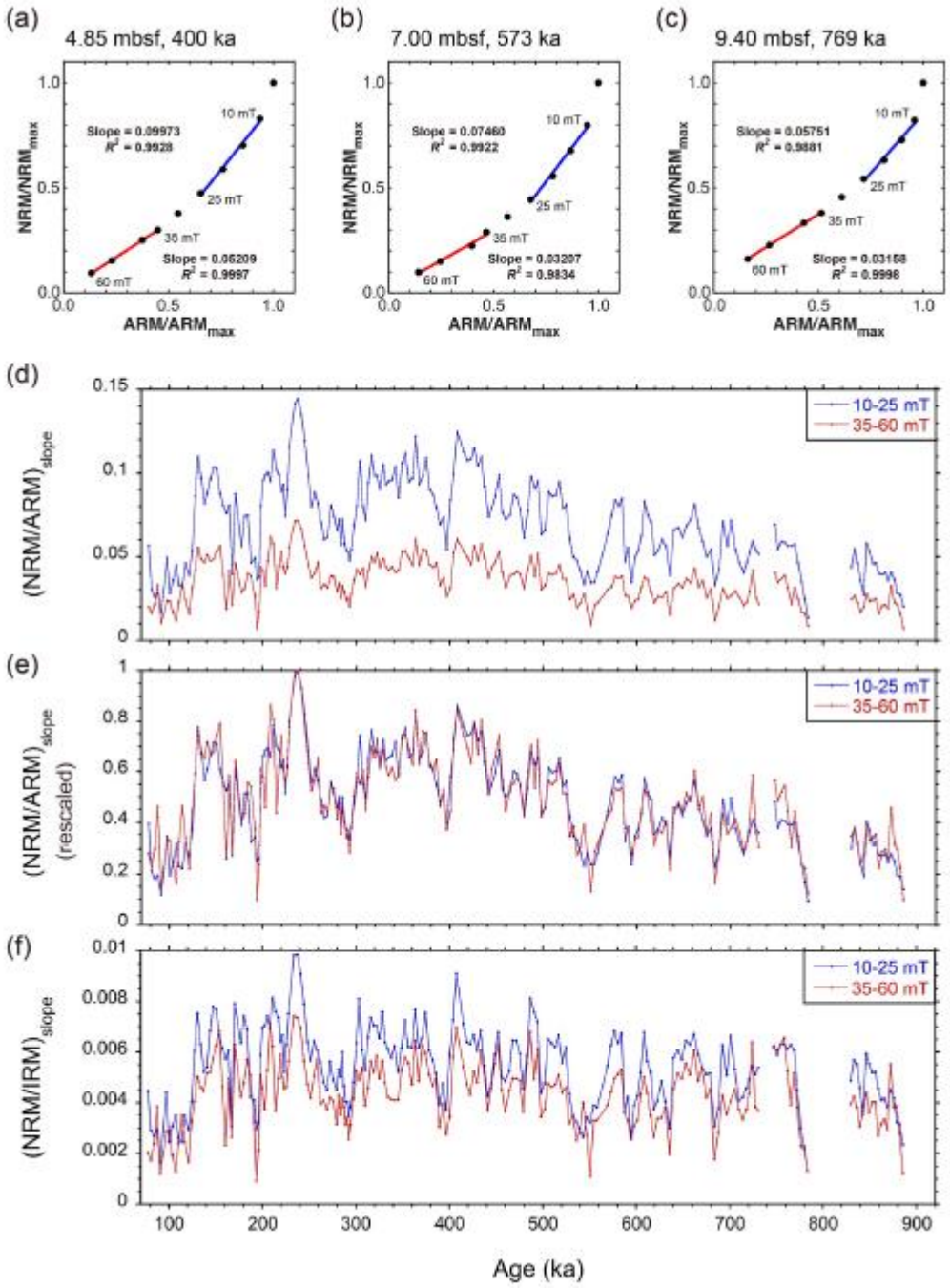

Figure 1. Examples of best-fit slopes for (a-c) NRM-ARM demagnetization diagrams calculated for AF demagnetization intervals of 10-25 mT (red lines) and 35-60 mT (blue lines). RPI signals calculated for the same coercivity windows for (d, e) NRM-ARM slope and (f) NRM-IRM slope. In panel (e) both RPI curves were normalized to their maximum values.

7. 德干火山作用认识进展

翻译人：张伟杰 12031188@mail.sustech.edu.cn

Self S, Mittal T, Dole G, et al. ***Toward Understanding Deccan Volcanism****[J]. Annual Review of Earth and Planetary Sciences, 2022, 50.*

https://doi.org/10.1146/annurev-earth-012721-051416

摘要：大火成岩省（LIPs）代表了地球历史上一些大型火山事件，其对生态系统产生重大影响，如大规模灭绝。然而，关于 LIP 熔岩流的喷发速率、喷发方式和喷口位置有关的一些基本问题仍然没有答案。德干大火成岩省是保存最完好的大型大陆溢流玄武岩省之一，在本文中，我们以白垩纪-古近纪德干大火成岩省为例来解决上述相关问题。我们描述了德干熔岩流的火山学特征、潜在的时间和区域变化以及潜在的补给岩墙的空间特征。结合古地磁学和汞记录估计的单个德干熔岩的平均长期喷发率约为 50-250 km^3/年（喷发数十至数百年），德干火山特征表明了一个统一的喷发概念模型-LIP 体积大（>1,000 km^3）、空间分布范围大（>40,000 km^2）。最后，我们强调了几个关键的开放性问题和挑战，这些问题和挑战可以帮助我们更好地理解德干火山流以及 LIP 火山流是如何爆发的，以及熔岩可能流过 1000 公里的机制。

ABSTRACT: Large igneous provinces (LIPs) represent some of the greatest volcanic events in Earth history with significant impacts on ecosystems, including mass extinctions. However, some fundamental questions related to the eruption rate, eruption style, and vent locations for LIP lava flows remain unanswered. In this review, we use the Cretaceous–Paleogene Deccan Traps as an archetype to address these questions because they are one of the best-preserved large continental flood basalt provinces. We describe the volcanological features of the Deccan flows and the potential temporal and regional variations as well as the spatial characteristics of potential feeder dikes. Along with estimates of mean long-term eruption rates for individual Deccan lavas from paleomagnetism and Hg proxy records of ~50–250 km^3/year (erupting for tens to hundreds of years), the Deccan volcanic characteristics suggest a unified conceptual model for eruption of voluminous (>1,000 km^3) LIP lavas with large spatial extent (>40,000 km^2). We conclude by highlighting a few

key open questions and challenges that can help improve our understanding of how the Deccan flows, as well as LIP flows in general, erupted and the mechanisms by which the lavas may have flowed over distances up to 1,000 km.

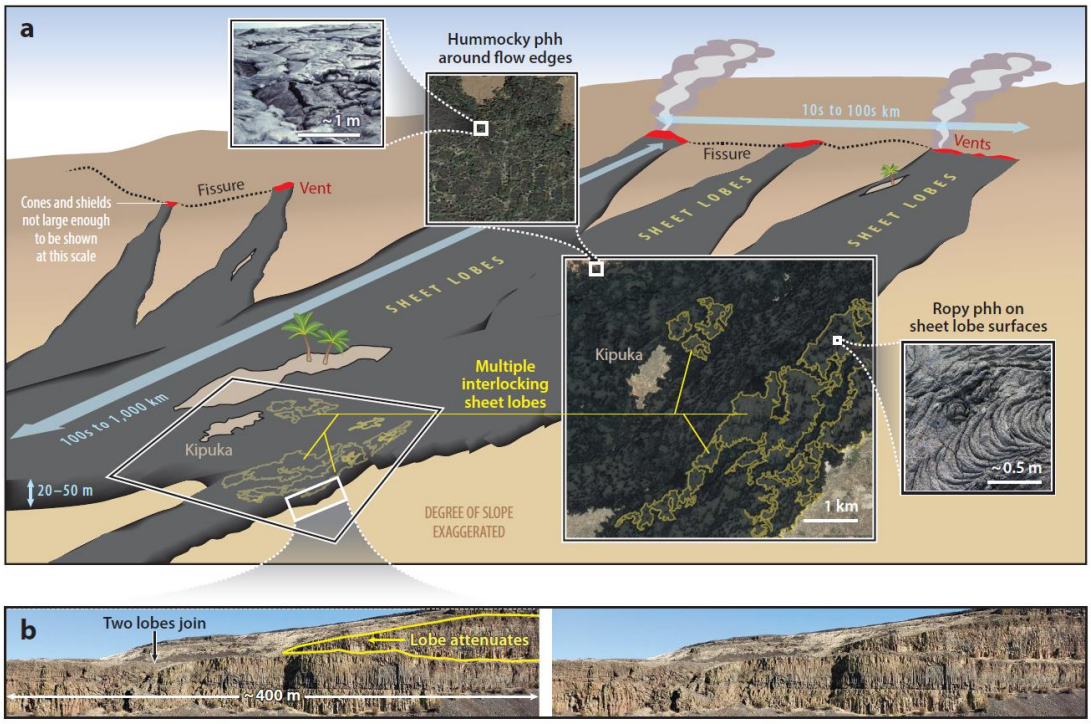

Figure 1. Structure and scale of a generic flood-lava pahoehoe (phh) flow field. (a) Diagram of theoretical Deccan-type phh flow field that could represent lavas from any formation. Proportion of hummocky-phh to sheet-lobe phh surfaces will change for different flow-fields between and within formations. Note that proximal zone is exaggerated in scale for clarity; note also that near-vent facies are known from the Columbia River Basalt province but are not described from the Deccan volcanic province. Aerial photo of Carrizozo, New Mexico, lava field from Google Earth. Lava surface detail photography fromWikipedia (CC BY-NC-ND 2.0) (right) and courtesy of Stephen Self 2001. (b) Section through sheet lobes in the Columbia River province showing a join (black arrow) between two lobes of the same flow (from top of talus to top of lobe on left is ~30 m, but bases of these lobes are buried in talus). A third sheet lobe of similar thickness thins to nothing (yellow outline). Photo courtesy of Stephen Self 2021. Exposures of such lobe contacts are difficult to find in the Deccan because of erosion, weathering, and poorer exposures.

8. 云在热带太平洋对温带热强迫的响应模式中的作用

翻译人：李海 12031330@mail.sustech.edu.cn

Hsiao W-T, Hwang Y-T, Chen Y-J, et al. ***The Role of Clouds in Shaping Tropical Pacific Response Pattern to Extratropical Thermal Forcing*** *[J]. Geophysical Research Letters, 2022, 49, e2022GL098023.*

https://doi.org/10.1029/2022GL098023

摘要：温带对热带海表温度（SST）年代际的预测存在影响。作者采用云锁定技术来强调云在塑造热带 SST 对温带热强迫的响应方面的关键作用。随着北大西洋或北太平洋上空的加热，哈德利 Cells 的反应类似于南部雨带的增强。风-蒸发-海温（WES）反馈导致南亚热带地区降温，由于 SST 和层状云之间的正反馈，东南太平洋的冷却增强。云锁定实验表明，太平洋海温的纬向对比和云反馈增强了纬向地表风，导致蒸发增加并加强了纬向 SST 差异。作者认为径向和纬向 SST 梯度通过 WES 效应和云-辐射-SST 反馈紧密联系，这在很大程度上取决于气候雨带位置和云特性的空间分布。

ABSTRACT: Extratropical influences on tropical sea surface temperature (SST) have implications for decadal predictability. We implement a cloud-locking technique to highlight the critical role of clouds in shaping the tropical SST response to extratropical thermal forcing. With heating imposed over either the extratropical Northern Atlantic or Pacific, Hadley Cells respond similarly that the trades strengthen south of the rainband. The wind-evaporation-SST (WES) feedback leads to cooling over the southern subtropics, which is enhanced in the southeastern Pacific due to the positive feedback between SST and stratiform clouds. Cloud-locking experiments show that zonal contrasts in SST and cloud feedbacks in the Pacific enhance the zonal surface winds, leading to increased evaporation and strengthens zonal SST difference. We propose that the meridional and zonal SST gradients are tightly linked via WES effects and the cloud-radiative-SST feedbacks, which are largely determined by the climatological rainband position and the spatial distribution of cloud properties.

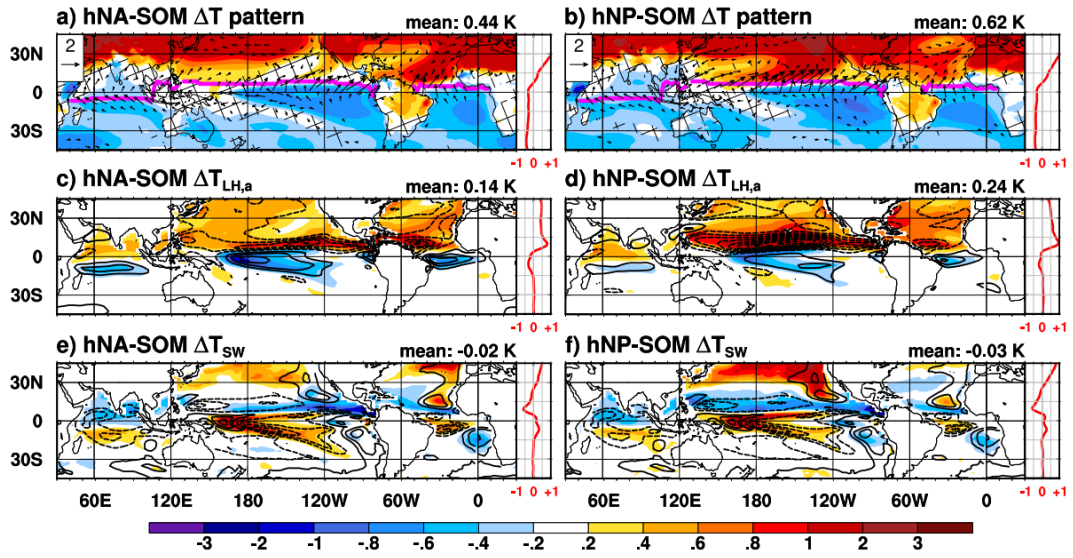

Figure 1. (a-b) responses of surface temperature pattern (shading; K) and 993-hPa winds (arrows), with climatological ITCZ defined at where the annual rainfall on marine region has meridional maxima (pink line), and the hatched regions show where the shading patterns are statistically insignificant at 5% level using two-tailed Student t-tests. In (c-d), shading shows $\Delta T_{LH;a}$ (units: K) and contours show the response of 10-meter wind speeds (spacing: 0.2 m s^{-1}). In (e-f), shading shows ΔT_{SW} (units: K) and contours show the surface SW-SST feedbacks estimated as the slope from the linear regression of surface shortwave radiative flux on SST using CTL-SOM (spacing: 5 W m^{-2} K^{-1}). The patterns of responses in (a-b) are calculated by removing their means over 30°S-30°N. Mean values of the shadings over 30°S-30°N are labeled, and zonal mean values of the shadings are attached on the right of each panel. For contours, dashed indicates negative, solid indicates positive, and zero lines are omitted.

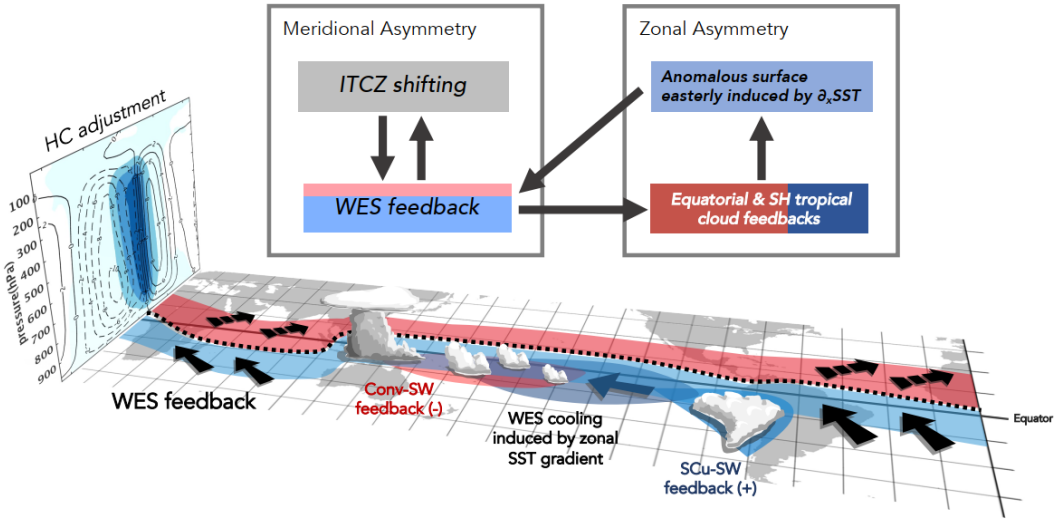

Figure 2. A schematic of the feedbacks behind the La Niña-like SST formation. Hadley Cell adjustment due to the forcing is shown on the left. On the map, the climatological ITCZ is indicated by the dashed line, with near-surface wind change (arrows) and associated SST change by the WES feedback (band-structured shading) when the ITCZ shifts north. Cloud-associated responses near the equator are also depicted with realistic style and its effects on SST response are as the shading patches. A flow chart of the discussed feedbacks is on the top, that the color patterns roughly indicate the spatial patterns of SST change that the feedbacks imposed, where blue colors are cooling and red colors are warming.

9. 50 万年来地球磁场、气候和轨道周期的多元统计分析及其在末次间冰期的关系

翻译人：张亚南 zhangyn3@mail.sustech.edu.cn

Cappellotto L, Julia M, Orgeira, M J, et al. ***Multivariable statistical analysis between geomagnetic field, climate, and orbital periodicities over the last 500 KYR, and their relationships during the last interglacial*** *[J]. Global and Planetary Change, 2022, 213, 103836.*

https://doi.org/10.1016/j.gloplacha.2022.103836

摘要：地磁场变化（GF）、古气候和米兰科维奇旋回之间的关系愈发受到研究人员的关注，主要是因为地磁场可能起着气候强迫的作用，地磁场变化和轨道强迫可能以一种复杂的协同方式联系在一起，特别是间冰期。文中作者首先详细分析了 50 万年来 GF、古温度指标、天文轨道参数和 65N°夏季日平均辐射之间的关系。并通过小波，交叉小波和多交叉小波分析变量之间在轨道周期上的关系，使得多个数据序列能够同时被分析并且确定信号之间的相对相位。作者证实了偏心率调节 GF 的变化，并且岁差可能与一些短期的 GF 变化有关。这两个轨道参数似乎都是 GF 变化的前兆。此外，GF 倒转事件可能是一种间接的气候强迫，因此对其作用的研究尤其有趣，作者重点研究了 MIS 5 时期各强迫之间的关系。在此期间，两次 GF 的倒转（Blake 和 post-Blake）可能与气候的相对变冷有关。GF 事件导致的地球磁场保护作用的减弱或缺失，以及太阳辐射的减少，最终促进了 MIS 5 期间全球气候的相对变冷。

ABSTRACT: Relationships between geomagnetic field (GF) variations, paleoclimates, and Milankovitch cycles have increasingly attracted the attention of researchers mainly because of the assumption that GF may have acted as a climate forcing, suggesting that GF variations and orbital forcing may be linked in a complex synergistic way, especially, during interglacials and interstadials. We first performed an exhaustive analysis of the relationship between GF, a paleotemperature proxy, astroclimatic parameters, and the summer solstice mean daily insolation at 65° N over the last 500 kyr. We evaluated the relationship between the variables at the orbital scale, using wavelets, cross

wavelets, and multiple cross wavelets. Our novel approach to the subject is the use of a new multiple cross wavelet algorithm, which allowed us to simultaneously analyze several data series and determine the relative phases between the signals. We confirm that the eccentricity modulates the GF behavior, and that the precession could have been related to some short-term GF variations. Both orbital parameters seem to be precursors of GF changes. Also, it is especially interesting to investigate the role of the GF reversion events because they could have acted as an indirect climate forcing, and we focused on the relationship among forcings during Marine Isotope Stage (MIS) 5. During this period, two GF reversions (Blake and post-Blake) could have been associated with relative climate cooling. The consequent lack or weakening of shielding associated with GF events and downward insolation, both influenced by orbital forcing, could finally have promoted a relative global climate cooling during MIS 5.

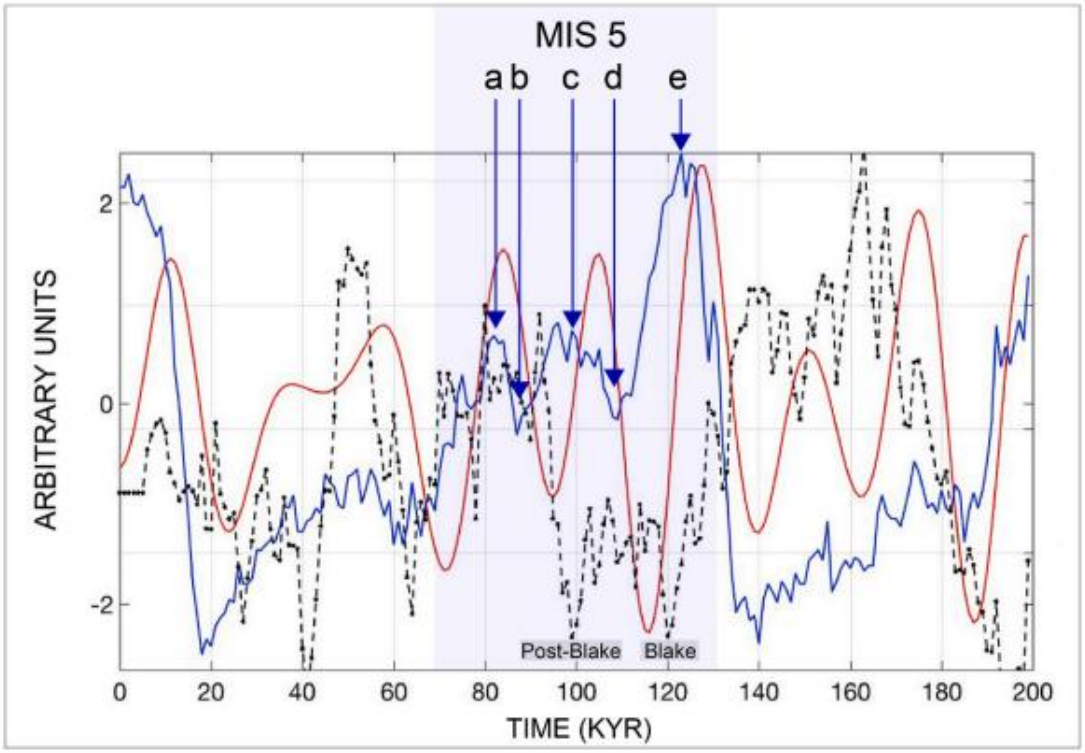

Figure 1. Detail of signals of $\delta^{18}O$ (blue line), RPI (black line), and mean daily insolation (red line). MIS 5 and its substages (a, b, c, d, and e) in the blue area. Blake and Post-Blake GF events in the gray area.

10. 旧石器-新石器过渡时期和冰后期以来气候变化：中国南方洞穴考古综述

翻译人：郑威 11930589@mail.sustech.edu.cn

Gorodetskaya O, Hsieh M L, Guo L X, et al. ***Paleolithic-Neolithic transition and late-to-postglacial climate change in East Asia: A review of archaeological data from karst caves in Southern China****[J].* ***Quaternary International****, 2022, 610: 20-37.*

https://doi.org/10.1016/j.quaint.2021.09.005

摘要：我们回顾了中国南方洞穴遗址旧石器晚期至新石器早期过渡阶段的考古学、年代学、生物学数据。我们的综述显示，放射性碳同位素年代的测试数量虽大，但与洞穴遗址已知的文化序列（基于遗物制造的复杂程度）并不一致，并且与生物学数据反映的古气候条件冲突。大多数的碳同位素年代比预期偏老，样本可能与地下水反应而吸收了死碳。我们认为，由生物学数据提供的年代框架比现有的放射性碳年代数据可以更为可靠的与古气候记录对应。因此，所有的新石器时期地层，及其中丰富的热带/亚热带和水生/亲水物种的生物遗迹很可能是全新世沉积的，而旧石器时期文化层可能可以追溯到新仙女木时期或波令-阿列罗德时期。我们的综述表明，冰后期以来的气候变化有助于东亚新石器文明的发展。我们将这一发展归因于气候暖湿期间溪流/湿地及其相关生态系统的增长（包括野生水稻的传播），这大大增加了可获取的食物、水和泥资源，使古人类有机会认识野生水稻、发明磨制石器和捏制陶器。

ABSTRACT: We review the archaeological, chronological, and biological data from multiple karst caves in southern China that date to the late-Paleolithic to early-Neolithic transition. Our review shows that the radiocarbon dates, although having a large quantity, do not align with the known cultural sequences correlated among the cave sites (based on the degree of sophistication of artefact manufacturing) and they conflict with the corresponding paleoclimatic conditions revealed by the biological data. Most of these radiocarbon dates are older than expected, and their samples probably incorporate dead carbon through the reaction with groundwater. We argue that, when correlated with global paleoclimate records, the chronological framework provided by the

biological datasets provides a more robust chronology than the available radiocarbon dates. Accordingly, all the Neolithic layers reviewed, with their plentiful biological remains of tropical/subtropical and aquatic/water-loving species, are likely to have been deposited in Holocene, and the Paleolithic cultural layers likely date to the Younger Dryas or the Bølling-Allerød. Our review suggests that the late-to-postglacial climate change helped initiate the development of Neolithic cultures in East Asia. We attribute this development to the growth of creeks/wetlands and their associated ecosystems (including the spreading of wild rice) during the period of climate warming and wetting, which greatly increased accessible food, water, and mud resources, providing opportunities for ancient peoples to recognize wild rice and to invent polishing stone tools and making pinched earthenware.

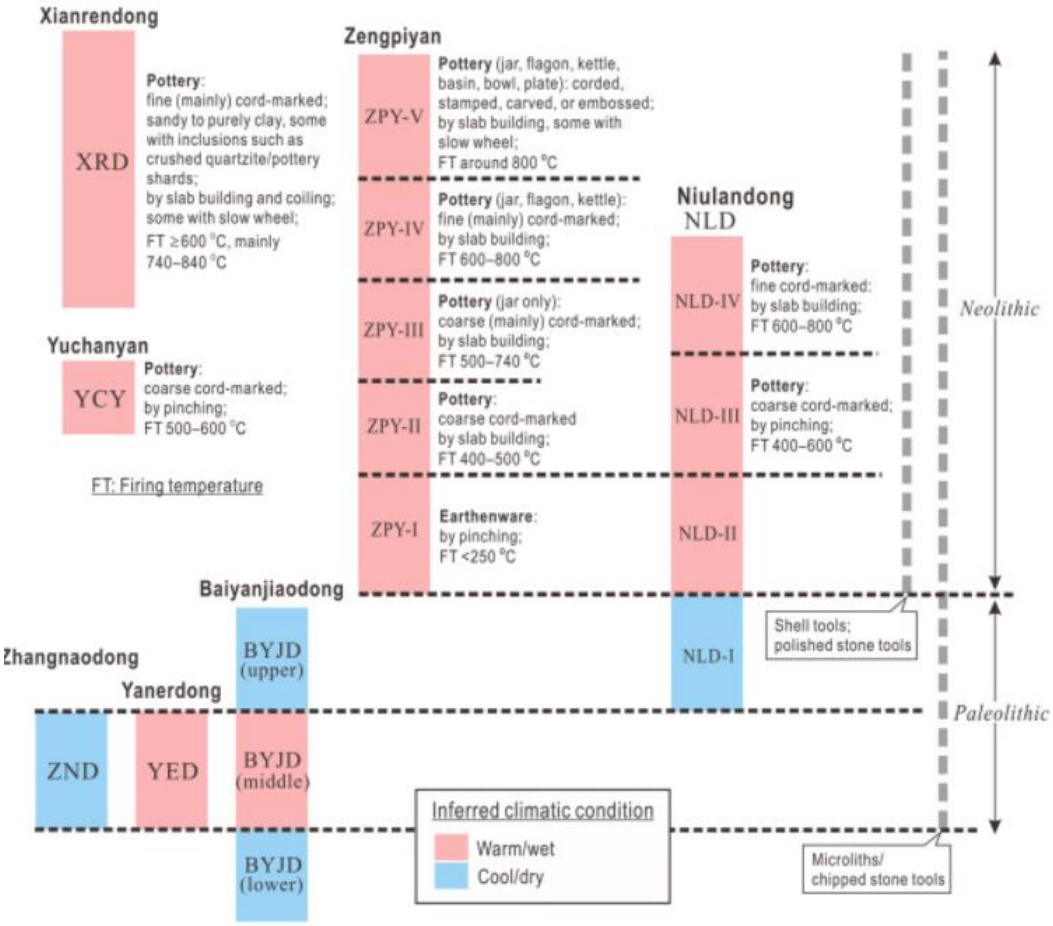

Figure 1. Correlation of cultural layers reviewed in this study, based on relative degrees of artefact manufacturing levels. Climate conditions inferred from assemblages of biological remains in the layers are also shown. For raw data see Table 2, Table 3.

11. 南海和大陆架珊瑚盐度重建的驱动因素：1976 年印太气候变化的影响

翻译人：刘宇星 11811211@mail.sustech.edu.cn

Kannad A, Goodkin N F, Samanta D, et al. ***Drivers of coral reconstructed salinity in the South China Sea and Maritime Continent: The influence of the 1976 Indo‐Pacific climate shift****[J]. Journal of Geophysical Research: Oceans, e2021JC017787.*

https://doi.org/10.1029/2021JC017787

摘要：太平洋水团经南海(SCS)和海洋陆架(MC)流入印度洋，在海洋温盐环流中发挥着重要作用，为低纬度海洋间的热盐交换提供了唯一的通道。南海和印度尼西亚径流的传输受东亚季风和与太平洋、印度洋相关的主要气候模式的调节。作为表层浮力的指标，海面盐度(SSS)对水体交换率至关重要，但 SSS 的仪器记录短且稀少。本文使用经验正交函数，利用基于珊瑚 $\delta^{18}O$ 重建的 SSS 研究气候变率对该地区长期 SSS 行为的作用。北方冬季和夏季 SSS 变率的主导模式响应了 1976 年印度-太平洋气候变化的影响。在数十年尺度上，只有东亚季风和印度洋偶极子(IOD)在 1976 年之后的冬季和夏季 SSS 中保留了它们的信号。在更高的频率下，冬季 SSS 从具有强烈的东亚季风信号转变为更具受 IOD 和厄尔尼诺南方涛动(ENSO)的变化影响。在夏季，在 1976 年之后仅观察到 ENSO 对 SSS 变率的影响发生了变化。IOD 和 ENSO 最近在推动 SCS 和 MC 中 SSS 变率方面的强化和主导地位可能会影响区域环流，甚至可能影响全球温盐环流。

ABSTRACT: The flow of Pacific water into the Indian Ocean via the South China Sea (SCS) and Maritime Continent (MC) plays an important role in the ocean thermohaline circulation providing the only low-latitude pathway for the inter-ocean exchange of heat and salt. The transport of the SCS and Indonesian throughflows is modulated by the East Asian monsoon and major climate modes associated with the Pacific and Indian Oceans. As an indicator of surface layer buoyancy, sea surface salinity (SSS) is critical to rates of exchange but instrumental records of SSS are short and sparse. Using empirical orthogonal functions, a synthesis of proxy-based reconstructions of SSS

from coral $\delta^{18}O$ is used to study the role of climate variability on long-term SSS behavior in the region. The leading mode of SSS variability in the boreal winter and summer responds to the influence of the 1976 Indo-Pacific climate shift. At multi-decadal timescales, only the East Asian monsoon and the Indian Ocean Dipole (IOD) retain their signal in winter and summer SSS after 1976. At higher frequencies, winter SSS shifts from having a strong East Asian monsoon signal to a more dominant impact of the IOD and the El Niño Southern Oscillation (ENSO) following the shift. In the summer, only a change in ENSO's influence on SSS variability is observed after 1976. The recent intensification and dominance of the IOD and ENSO in driving SSS variability in the SCS and MC may influence circulation in the regional throughflows and perhaps global thermohaline circulation.

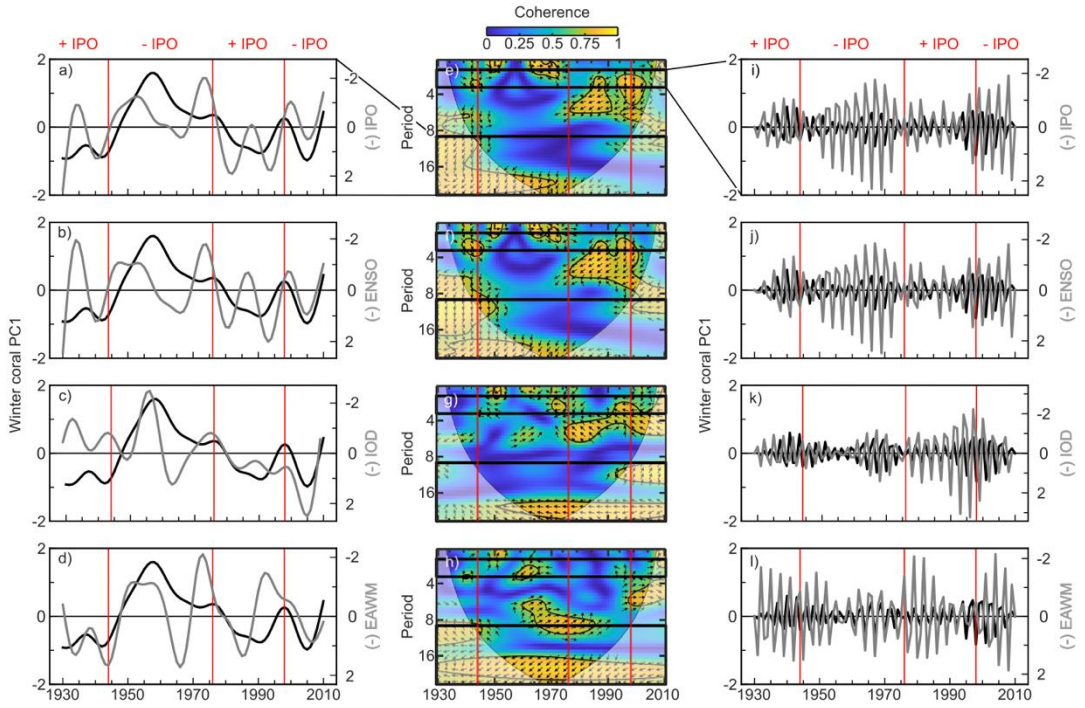

Figure 1. Comparison of winter coral sea surface salinity (SSS) PC1 and climate indices. Low-pass filtered (>9.8 yr) winter PC1 (black solid line) with similarly filtered climate indices (gray solid line) of (a) IPO, (b) ENSO, (c) IOD, and (d) EAWM highlight SSS and climate variability at frequencies describing regional processes. Similarly, winter PC1 (black solid line) at interannual frequencies (2.5–3.5 yr) is compared to filtered (i) IPO, (j) ENSO, (k) IOD, and (l) EAWM (all gray solid line). The axes for the climate indices are inverted. Time-varying coherence is examined using wavelet analyses of coral winter PC1 and (e) IPO, (f) ENSO, (g) IOD, and (h) EAWM. The filtered frequencies in panels (a–d and i–l), which represent regional variability, are indicated with black boxes in panels (e–h). Contours (black) in panels (e–h) indicate the 95% confidence level determined against the red noise null hypothesis and arrows denote the relative phase relationships. The cone of influence is shown in a lighter shade. For both methods of comparison, the important phase shifts of the IPO in 1944, 1976, and 1998 (England et al., 2014) and the 1976 Indo-Pacific climatic shift are marked with red vertical lines.

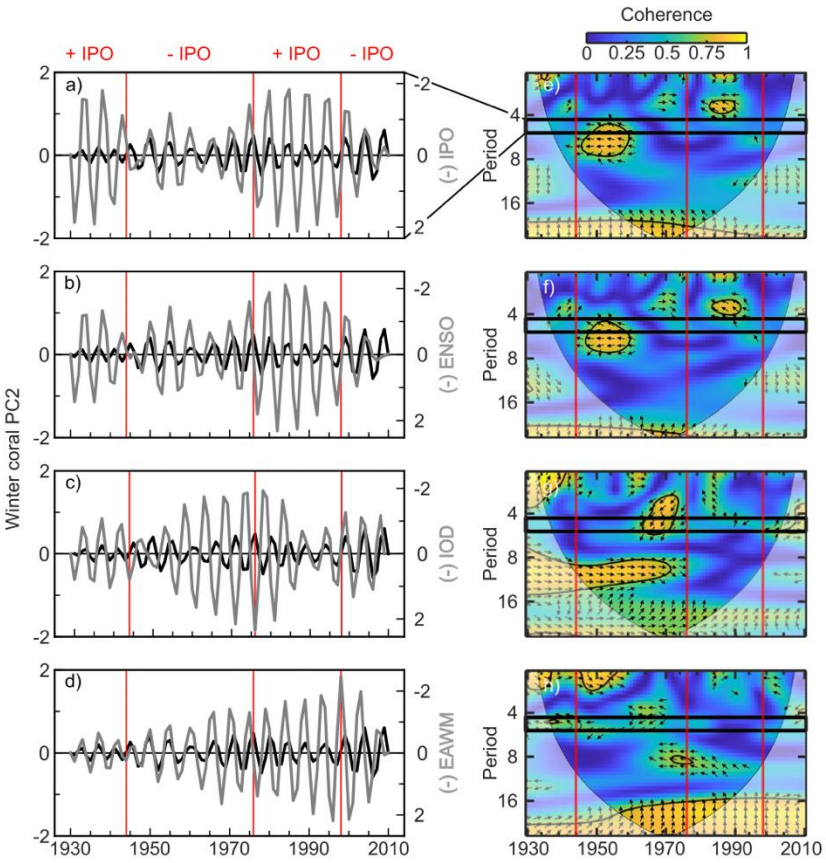

Figure 2. Comparison of winter coral sea surface salinity (SSS) PC2 and climate indices. Band-pass filtered (4.3–5.3 yr) winter PC2 (black solid line) with similarly filtered climate indices (gray solid line) of (a) IPO, (b) ENSO, (c) IOD, and (d) EAWM highlight SSS and climate variability at frequencies describing regional processes. The axes for the climate indices are inverted. Time-varying coherence is examined using wavelet analyses of coral winter PC2 and (e) IPO, (f) ENSO, (g) IOD, and (h) EAWM. The filtered frequencies in panels (a–d) are indicated with black boxes in panels (e–h). Contours (black) in panels (e–h) indicate the 95% confidence level determined against the red noise null hypothesis and arrows describe relative phase relationships. The cone of influence is shown in a lighter shade. For both methods of comparison, the important phase shifts of the IPO in 1944, 1976, and 1998 (England et al., 2014) and the 1976 Indo-Pacific climatic shift are marked with red vertical lines.

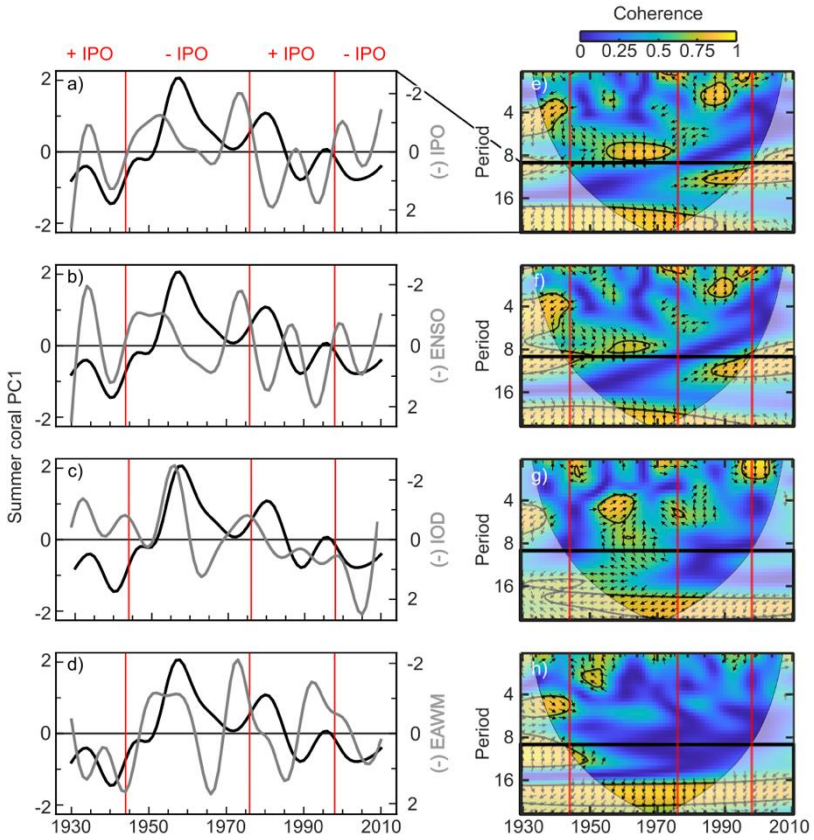

Figure 3. Comparison of summer coral sea surface salinity (SSS) PC1 and climate indices. Low-pass filtered (>9.8 yr) summer PC1 (black solid line) with similarly filtered climate indices (gray solid line) of (a) IPO, (b) ENSO, (c) IOD, and (d) EAWM highlight SSS and climate variability at frequencies describing regional processes. The axes for the climate indices are inverted. Time-varying coherence is examined using wavelet analyses of coral summer PC1 and (e) IPO, (f) ENSO, (g) IOD, and (h) EAWM. The filtered frequencies in panels (a–d) are indicated with black boxes in panels (e–h). Contours (black) in panels (e–h) indicate the 95% confidence level determined against the red noise null hypothesis and arrows describe relative phase relationships. The cone of influence is shown in a lighter shade. For both methods of comparison, the important phase shifts of the IPO in 1944, 1976, and 1998 (England et al., 2014) and the 1976 Indo-Pacific climatic shift are marked with red vertical lines.

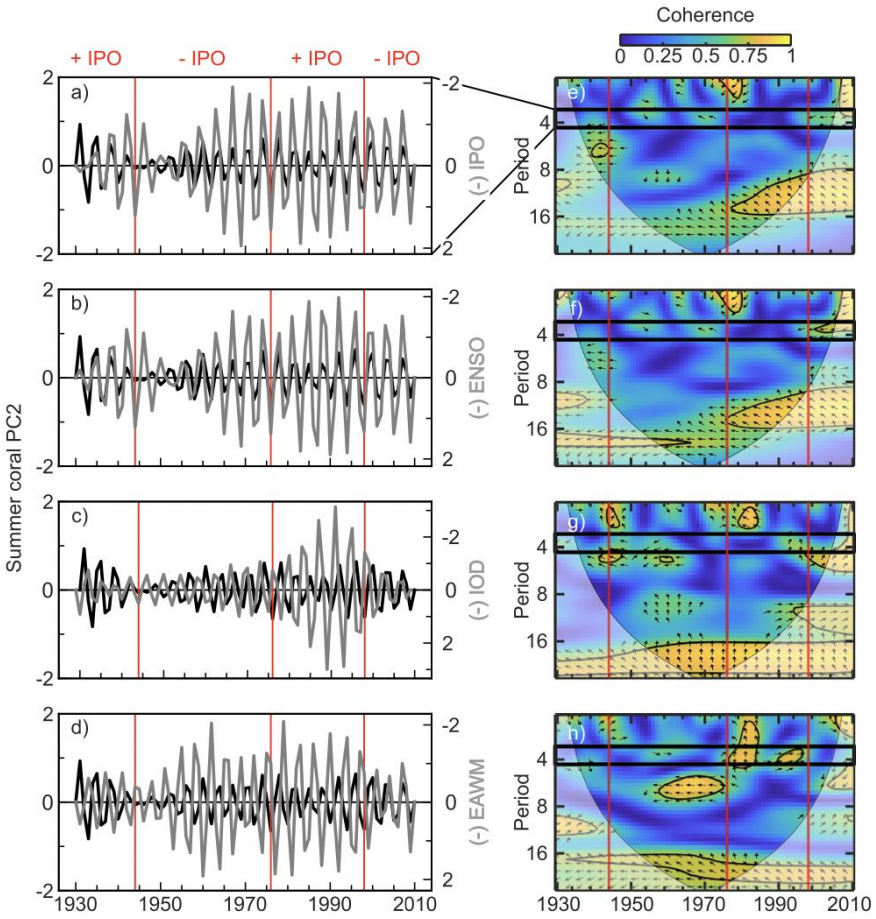

Figure 4. Comparison of summer coral sea surface salinity (SSS) PC2 and climate indices. Band-pass filtered (3.3–4.3 yr) summer PC2 (black solid line) with similarly filtered climate indices (gray solid line) of (a) IPO, (b) ENSO, (c) IOD, and (d) East Asian winter monsoon (EAWM) highlight SSS and climate variability at frequencies describing regional processes. The axes for the climate indices are inverted. Time-varying coherence is examined using wavelet analyses of coral winter PC1 and (e) IPO, (f) ENSO, (g) IOD, and (h) EAWM. The filtered frequencies in panels (a–d) are indicated with black boxes in panels (e–h). Contours (black) in panels (e–h) indicate the 95% confidence level determined against the red noise null hypothesis and arrows describe relative phase relationships. The cone of influence is shown in a lighter shade. For both methods of comparison, the important phase shifts of the IPO in 1944, 1976, and 1998 (England et al., 2014) and the 1976 Indo-Pacific climatic shift are marked with red vertical lines.